



Research paper

3D magnetotelluric modeling using high-order tetrahedral Nédélec elements on massively parallel computing platforms

Octavio Castillo-Reyes^{a,*}, David Modesto^a, Pilar Queralt^b, Alex Marcuello^b, Juanjo Ledo^b, Adrian Amor-Martin^c, Josep de la Puente^a, Luis Emilio García-Castillo^c

^a Barcelona Supercomputing Center (BSC), c/Jordi Girona, 29. 08034, Barcelona, Spain

^b Institut Geomodels, Departament de Dinàmica de la Terra i de l'Oceà, University of Barcelona, c/Martí Franqués s/n. 08028, Barcelona, Spain

^c Department of Signal Theory and Communications, University Carlos III of Madrid, c/de la Universidad, 30. 28903, Madrid, Spain

ARTICLE INFO

Keywords:

Magnetotelluric method
Geophysical electromagnetics
Numerical solutions
High-order edge finite element
High-performance computing

ABSTRACT

We present a routine for 3D magnetotelluric (MT) modeling based upon high-order edge finite element method (HEFEM), tailored and unstructured tetrahedral meshes, and high-performance computing (HPC). This implementation extends the PETGEM modeller capabilities, initially developed for active-source electromagnetic methods in frequency-domain. We assess the accuracy, robustness, and performance of the code using a set of reference models developed by the MT community in well-known reported workshops. The scale and geological properties of these 3D MT setups are challenging, making them ideal for addressing a rigorous validation. Our numerical assessment proves that this new algorithm can produce the expected solutions for arbitrarily 3D MT models. Also, our extensive experimental results reveal four main insights: (1) high-order discretizations in conjunction with tailored meshes can offer excellent accuracy; (2) a rigorous mesh design based on the skin-depth principle can be beneficial for the solution of the 3D MT problem in terms of numerical accuracy and run-time; (3) high-order polynomial basis functions achieve better speed-up and parallel efficiency ratios than low-order polynomial basis functions on cutting-edge HPC platforms; (4) a triple helix approach based on HEFEM, tailored meshes, and HPC can be extremely competitive for the solution of realistic and complex 3D MT models and geophysical electromagnetics in general.

1. Introduction

The 3D magnetotelluric (MT) is a sounding technique to obtain the electrical resistivity distribution of the subsurface from simultaneous measurement of naturally induced electromagnetic (EM) fields in the Earth's subsurface. The EM response to the natural excitation sources depends on the electrical resistivity of the geological structures. From this dependence, it is possible to extract useful subsurface information to improve and reinforce geophysical characterization and interpretation. As a result, the 3D MT method has been widely used to mapping subsurface conductivity/resistivity variations at different scales (e.g., from lithospheric and crustal to near surface studies Ledo et al., 2002; Campanyà et al., 2012) and in diverse geophysical applications (e.g., hydrocarbon exploration, mineral mining, CO₂ sequestration, geothermal reservoir characterization Queralt et al., 2007; Vilamajó et al., 2013; Piña-Varas et al., 2015).

Geophysics EM modeling is an active research area, and several 3D modelers have been developed to study and understand MT responses. For the solution of Maxwell's equations, these modeling routines are

typically based on four major numerical approaches: integral equation (IE; Colton and Kress, 2013), finite difference (FD; Kunz and Luebbers, 1993), finite volume (FV; Eymard et al., 2000), and finite elements (FE; Jin, 2015).

One of the first attempts of 3D MT modeling using the IE method dates to the 1980s, when Ting and Hohmann (1981) presented their results for the solution of theoretical surface anomalies because to 3D conductive bodies buried in a half-space Earth. Other applications of the IE method for 3D MT modeling were presented by Wannamaker (1991) and Avdeeva et al. (2015). In all of them, the IE method results in a dense linear system of equations and works efficiently for simple layered models. However, its major drawback is the expensive computational cost when the model complexity increases (e.g., models with several layers).

The FD method arises as one of the most commonly used approaches for 3D MT modeling. Its main advantage is the comparably reduced implementation effort. On the other hand, the major disadvantage of FD schemes is their inability to work on unstructured meshes. As a

* Corresponding author.

E-mail address: octavio.castillo@bsc.es (O. Castillo-Reyes).

<https://doi.org/10.1016/j.cageo.2021.105030>

Received 15 June 2021; Received in revised form 27 December 2021; Accepted 30 December 2021

Available online 15 January 2022

0098-3004/© 2022 The Author(s). Published by Elsevier Ltd. This is an open access article under the CC BY license (<http://creativecommons.org/licenses/by/4.0/>).

result, FD methods can only approximate complex geometries using a stair-case strategy. FD modeling algorithms for MT datasets are those developed by Mackie et al. (1994), Siripunvaraporn et al. (2002), Kun et al. (2013), Kelbert et al. (2014), Singh et al. (2017), Variltsuha and Candansayar (2018), among others.

Like the FD approach, the FV scheme combines the advantages of a straightforward mathematical formulation and computational implementation. Given its reduced implementation effort, the FV method has recently been employed for 3D MT modeling, either for 2D problems on arbitrary topographies (e.g., Du et al., 2016) or 3D Earth models with general anisotropy (e.g., Guo et al., 2020). But, although it supports unstructured grids, the accuracy of FV solutions is, in general, inferior to FE computations when comparing meshes with similar characteristics (Bondeson et al., 2012; Jahandari et al., 2017).

The FE method can overcome the issue mentioned above regarding structured grids due it has full flexibility concerning complex geometrical structures using unstructured grids. Also, the FE schemes offers a good trade-off between accuracy and the number of degrees of freedom (dof). One of the early challenges of EM modeling using FE was the possible jump of normal components across material interfaces (Börner, 2010). The nodal-based FE cannot reproduce the physical behavior of field discontinuities, leading to spurious solutions (Jin, 2015). The introduction of edge FE, also referred to as Nédélec elements (Nédélec, 1980), resolved this issue. The edge FE family provides stable numerical solutions through proper discretization of the *curl* space to which the EM field belongs. The basis functions of edge elements can perfectly treat EM fields' discontinuities across material interfaces (e.g., ensuring tangential continuity of the fields, while the normal components are allowed to be discontinuous). Also, since edge elements belong to the FE class, the accuracy of the solution can be extremely improved by using adaptive mesh refinement (*h*-refinement) and polynomial degree refinement (*p*-refinement). Considering its advantages for EM fields, the edge FE method has recently been employed for 3D MT modeling, either using hexahedral meshes (e.g., Nam et al., 2007, 2008; Farquharson and Miensopust, 2011; Kordy et al., 2016; Rivera-Rios et al., 2019; Zhang et al., 2021) or tetrahedral meshes (e.g., Liu et al., 2008; Nam and Kim, 2010; Xiao et al., 2018; Zhu et al., 2021). However, with the sole exception of the algorithms developed by Rivera-Rios et al. (2019) and Grayver and Kolev (2015) none support high-order edge vector basis, and they are either sequential or black-box packages. Also, only modeling routines implemented by Kordy et al. (2016) and Zhu et al. (2021) supports parallel computations on modest multi-core architectures.

This paper presents a high-order edge FE method (HEFEM) algorithm for the efficient solution of arbitrary 3D MT modeling problems under anisotropic conductivities. To model realistic-world 3D MT datasets, our modeling tool supports tailored and unstructured tetrahedral meshes (*h*-refinement), high-order polynomial variants (global *p*-refinement for $p = 1, 2, 3, 4, 5, 6$), and massively parallel computations. Also, we investigate the impact of mesh quality on the EM responses by testing our previously published meshing rules in Castillo-Reyes et al. (2019), where a tetrahedral adaptive-meshing strategy has been developed and studied over controlled-source electromagnetic method (CSEM) scenarios. Our implementation is based on and extends the Parallel Edge-based Tool for Geophysical EM Modeling (PETGEM; Castillo-Reyes et al., 2018). With the inclusion of this new high-order 3D MT routine, the upgraded PETGEM is well suited to simulate 3D MT/CSEM survey data on realistic models containing dipping layers, large conductivity/resistivity contrasts, multiple-scale structures, and wide range of periods.

The rest of the paper is organized as follows. Section 2 provides a comprehensive description about the mathematical background of our modeling routine. In Section 3, we perform PETGEM simulations for challenging 3D MT setups presented in the literature and analyze their EM responses versus numerical tests. In Section 4, we discuss important points to control the performance and suitability of our modeling tool, including considerations about the mesh design. Finally, Section 5 provides summary remarks.

2. Problem statement

The 3D MT method is mathematically described in spatial coordinates $\mathbf{x} \in \Omega$ by the frequency-domain Maxwell's equations in diffusive form, written as

$$\nabla \times \mathbf{E} = i\omega\mu\mathbf{H} + \mathbf{K}, \quad (1)$$

$$\nabla \times \mathbf{H} = \mathbf{J} + (\sigma + i\omega\epsilon)\mathbf{E}, \quad (2)$$

where \mathbf{E} , \mathbf{H} and \mathbf{J} , \mathbf{K} are the electric and magnetic fields and sources respectively; i is the imaginary unit; ω is the angular frequency; μ is the magnetic permeability for Earth materials (Chave and Jones, 2012); ϵ denotes the constant model permittivity; and σ is the variable electric conductivity tensor. Fig. 1 depicts a sketch of the computational domain Ω .

When MT methods are considered, natural electric and magnetic fields of the Earth subsurface are measured and no external sources are generated, thus $\mathbf{K} = \mathbf{J} = \mathbf{0}$. Imposing additionally the usual assumption $\sigma \gg \omega\epsilon$, Eqs. (1) and (2) can be rewritten only in terms of the electric field using the Helmholtz form of the Maxwell's equations, that is

$$\nabla \times \nabla \times \mathbf{E} - i\omega\mu\sigma\mathbf{E} = \mathbf{0} \quad \text{in } \Omega. \quad (3)$$

The approximation of the electric field by the HEFEM requires the variational (weak) form of Eq. (3). Let us define the space of curl-conforming basis functions that we use for the approximation of \mathbf{E} as

$$\mathbf{H}(\text{curl}, \Omega) := \{ \mathbf{w} \in [L_2(\Omega)]^3 \mid \nabla \times \mathbf{w} \in [L_2(\Omega)]^3 \}. \quad (4)$$

We follow the Galerkin method (Jin, 2015), testing with an appropriate weighting function $\mathbf{v} \in \mathbf{H}(\text{curl}, \Omega)$ over the whole Ω , so

$$\int_{\Omega} \mathbf{v} \cdot (\nabla \times \nabla \times \mathbf{E} - i\omega\mu\sigma\mathbf{E}) \, d\Omega = 0. \quad (5)$$

Taking into account the vector calculus identities

$$\mathbf{v} \cdot (\nabla \times \mathbf{F}) = \mathbf{F} \cdot (\nabla \times \mathbf{v}) + \nabla \cdot (\mathbf{F} \times \mathbf{v}), \quad (6)$$

$$\mathbf{n} \cdot (\mathbf{F} \times \mathbf{v}) = \mathbf{v} \cdot (\mathbf{n} \times \mathbf{F}), \quad (7)$$

with $\mathbf{F} = \nabla \times \mathbf{E}$ and \mathbf{n} as the outward-pointing normal to a surface, and using the divergence theorem on the resulting divergence term, finally yields, for all the test functions $\mathbf{v} \in \mathbf{H}(\text{curl}, \Omega)$, the weak form

$$a(\mathbf{E}, \mathbf{v}) = l(\mathbf{v}), \quad (8)$$

with bilinear form $a(\cdot, \cdot)$ and linear form $l(\cdot)$ defined by

$$a(\mathbf{E}, \mathbf{v}) = \int_{\Omega} (\nabla \times \mathbf{v}) \cdot (\nabla \times \mathbf{E}) - i\omega\mu\sigma\mathbf{v} \cdot \mathbf{E} \, d\Omega, \quad (9)$$

$$l(\mathbf{v}) = -i\omega\mu \int_{\Gamma} \mathbf{v} \cdot (\mathbf{n} \times \hat{\mathbf{H}}) \, d\Gamma, \quad (10)$$

where $\hat{\mathbf{H}}$ is the magnetic field imposed on the boundary Γ of the domain. Note from Fig. 1 that $\Gamma = \partial\Omega = \bigcup_{i=1}^6 \Gamma_i$.

2.1. Boundary conditions

The boundary conditions for the MT problem in Eq. (8) are generated by specifying the value of the magnetic field $\hat{\mathbf{H}}$ imposed on each surface Γ_i , $i = 1, \dots, 6$, see Fig. 1, and then computing the integral term in Eq. (10). Given that usual quantities of interest for MT applications (e.g., apparent resistivity) require the computation of the model impedance, both electric *x*-polarization and *y*-polarization computations are required, see Appendix A for more details. These modes impose a magnetic field $\hat{\mathbf{H}} = [0, \hat{H}(z), 0]$ and $\hat{\mathbf{H}} = [\hat{H}(z), 0, 0]$ for the *x* and *y*-polarization case respectively.

Without loss of generality, a constant value $\hat{H} = 1$ is imposed on the surface Γ_1 (see Fig. 1) because only the ratio between electric and magnetic fields determines the impedance property. Also, the natural damping of the EM field imposes $\hat{H} = 0$ on Γ_6 . On both surfaces

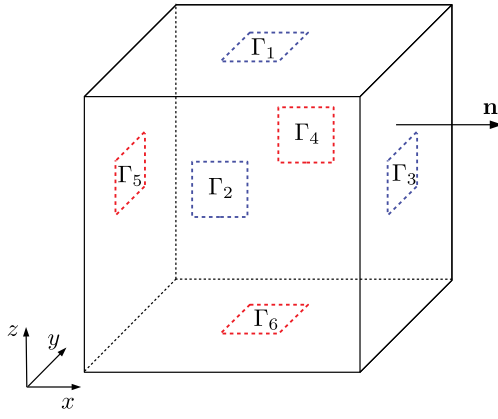


Fig. 1. Sketch of the computational domain Ω and its boundary surfaces $\Gamma_1, \dots, \Gamma_6$.

Γ_1 and Γ_6 (i.e., air and deep subsoil layers respectively) the model conductivity is assumed to be constant. On the rest of surfaces, the conductivity is considered variable only along the z coordinate and the scalar magnetic component $\hat{H}(z)$ is evaluated by solving the 1D Maxwell's model particularized as

$$\begin{aligned} \frac{d^2 \hat{H}(z)}{dz^2} + i\omega\mu\sigma(z)\hat{H}(z) &= 0 \quad \text{in } (z_{\min}, z_{\max}), \\ \hat{H}(z_{\max}) &= 1, \\ \hat{H}(z_{\min}) &= 0, \end{aligned} \quad (11)$$

where, for a given surface, z_{\min} and z_{\max} are the lower and higher values of the z coordinate respectively, and $\sigma(z)$ corresponds to the vertical conductivity profile. For more concise details on the computation of the integration terms in Eqs. (9) and (10) using the HEFEM, see Appendix B.

3. Numerical validation

To verify the robustness of the upgraded PETGEM version, we simulate different and relevant scenarios of the 3D MT problem. We chose some of the models that the MT community has developed in the frame of several workshops: *mt3dinv1* (Dublin-2008), *mt3dinv2* (Dublin-2011), and *mt3dinv3* (Bari2016). The main results of the chosen models are reported and discussed in Miensopust et al. (2013). Also, in the corresponding workshop web-page, several synthetic MT responses can be downloaded for comparison purposes. Each model presents a particular numerical modeling challenge, being a suitable approach to study the code capabilities (e.g., discretization of boundaries, mesh quality, run-time). In the next sections, we will discuss the most relevant cases. Further, readers interested in the complete set of PETGEM solutions are referred to Section ‘‘Code and data availability’’.

From the computational point of view, we use a standard continuous FE approximation for solving the 1D Eq. (11) with an element size 10 times smaller than the one used in HEFEM for solving the 3D model in Eq. (8). For all test cases, we use Gmsh (Geuzaine and Remacle, 2008) to perform the tailored mesh generation. This process is based on the strategy proposed by Castillo-Reyes et al. (2019) and accomplished using simple Python scripts and calls to routines from Gmsh. We use the multifrontal solver MUMPS (Amestoy et al., 2006) to solve the proposed 3D MT setups and study the parallel scalability of the code. This solver is supported by PETGEM via the PETSc interface (Balay et al., 2016). Furthermore, in all experiments, we consider run-time as the elapsed real-world time from start to end of assembling and solving the sparse linear system. Memory refers to the maximum peak of memory consumption at any point of solving region. All simulations have been performed on *Marenostrum IV* supercomputer using 240 CPUs.

Table 1

Mesh statistics for the 3D trapezoidal hill model. The number of skin-depths n_δ , model dimensions, number of tetrahedral elements, and number of dof are given. Two different orders of polynomial basis functions have been used ($p = 1, 2$).

n_δ	Model dimensions (km)	$p = 1$		$p = 2$	
		Elements	dof	Elements	dof
1	$[-5.5, 5.5]^3$	330 322	385 713	157 692	1 001 658
2	$[-9, 9]^3$	350 640	409 093	166 485	1 057 078
4	$[-16, 16]^3$	378 499	442 483	170 869	1 091 046
6	$[-23, 23]^3$	416 394	488 402	197 900	1 267 734
8	$[-30, 30]^3$	462 918	544 245	231 176	1 484 786
10	$[-37, 37]^3$	518 484	610 643	266 356	1 712 398

3.1. Tailored meshes for a 3D hill model

As the first example, we investigate the performance of our tailored meshing strategy using high-order edge elements. The purpose of this experiment is to validate our implementation and determine a suitable approach for the truncation of the computational domain, which is usually large enough so that the approximate solution at the boundaries matches the reference solution (i.e., determining how many skin-depths (δ) are required for the boundary to be sufficiently far away from the inhomogeneities in every direction). Therefore, we perform a set of simulations to study the impact of tailored meshes and how they can significantly reduce the computational domain size.

We consider the 3D trapezoidal hill model introduced by Nam et al. (2007), which is a homogeneous half-space model with $\rho_{\text{earth}} = 100 \Omega \text{ m}$ as host resistivity and $\rho_{\text{air}} = 1 \times 10^8 \Omega \text{ m}$ as the free-space resistivity. The trapezoidal hill, centered at the computational domain, has a height of 0.45 km with a hill-top square of $0.45 \times 0.45 \text{ km}$, and a hill-bottom square of $2 \times 2 \text{ km}$. A cross-section view of the model under consideration is depicted in Fig. 2. By using the horizontal components of the EM fields at 2 Hz, we compute the apparent resistivities for $p = 1, 2$. The ρ_{xy} and ρ_{yx} components. 41 sites at $y = 0 \text{ km}$ and along the x -axis are arranged equidistant spacing over the interval $x = [-2, 2] \text{ km}$.

3.1.1. Impact of boundaries placed at different number of skin-depths

As the first part of this test, we truncate the computational domain using different number of skin-depths (n_δ) and study its impact on the accuracy of the obtained EM responses. For this model, the skin-depth is approximately $\delta = 3.5 \text{ km}$ in terms of the host resistivity of ρ_{earth} . Based on this parameter, we design a set of tailored meshes for $p = 1, 2$. In particular, twelve numerical solutions have been computed on different meshes using $n_\delta = 1, 2, 4, 6, 8, 10$ and $p = 1, 2$, respectively. The resulting mesh hierarchies are shown in Table 1.

The obtained apparent resistivities (ρ_{xy} and ρ_{yx}) and phases (ϕ_{xy} and ϕ_{yx}) for $p = 1, 2$ are shown in Fig. 3. A close inspection of both numerical approximations allows us to observe two patterns in the EM responses. First, the apparent resistivities and phases at measuring stations located far from the hill, corresponds to the solution of a homogeneous flat Earth model (e.g., apparent resistivity of $100 \Omega \text{ m}$ with phase of 45°). Second, for stations located over the hill-top, the apparent resistivities and phases are significantly altered by the presence of the surface topography slope. More concretely, the apparent resistivity component ρ_{xy} shows oscillations while for the resistivity component ρ_{yx} decreases. The phases over the hill-top are about 5° higher in comparison with that obtained over the hill-base. This general EM behavior is consistent with other low-order FE solutions previously published (Nam et al., 2007, 2008; Ren et al., 2013; Zhu et al., 2021). However, we point out that although both orders of polynomial basis functions can obtain the EM mapping as expected, the $p = 2$ produces better numerical solutions than $p = 1$ (e.g., EM fields obtained with $p = 2$ are less oscillating and closer to the theoretical definition).

Additionally, we consider an L^2 -norm to quantify the errors (ϵ) of each numerical approximation with respect to a reference solution computed on a very h -fine mesh with $p = 6$ and outer boundaries

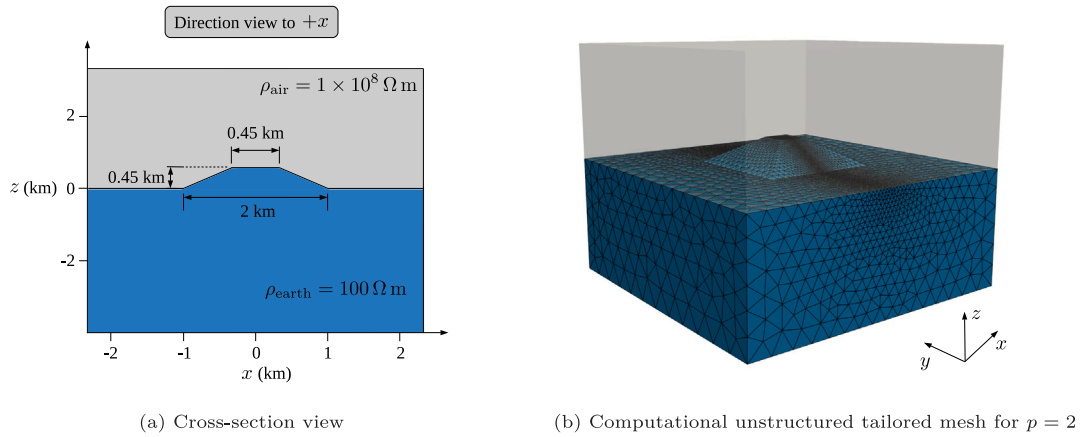


Fig. 2. 3D trapezoidal hill model by Nam et al. (2007).

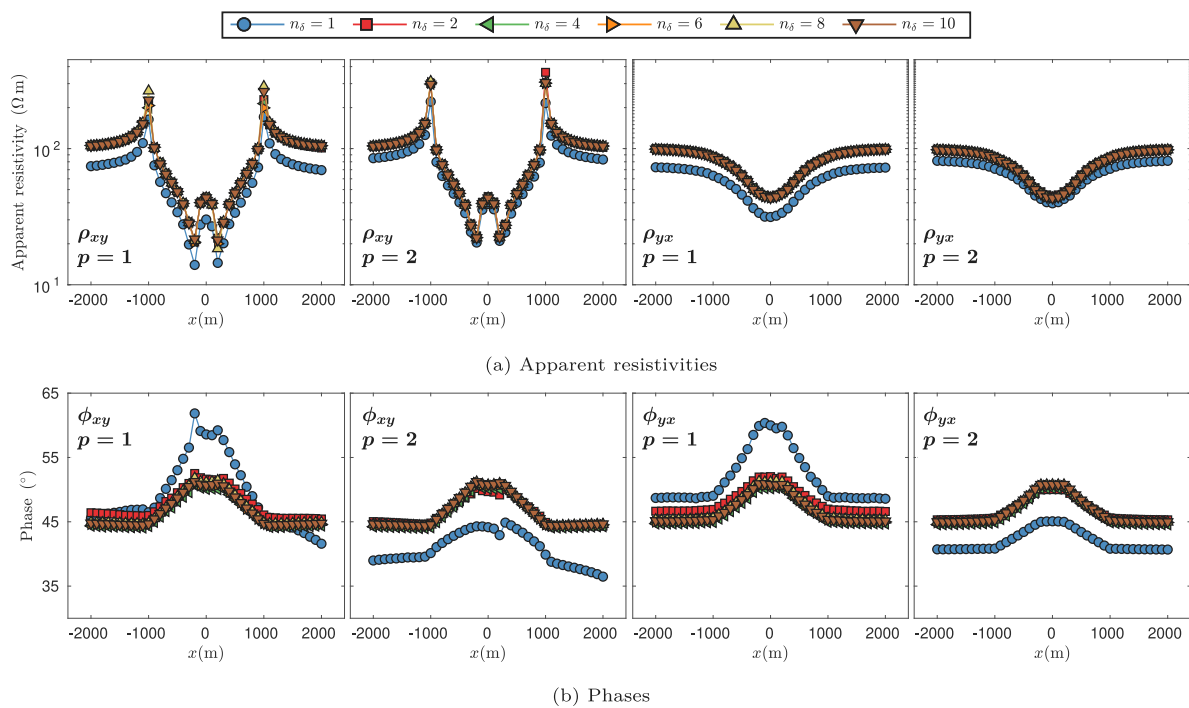


Fig. 3. Comparison of MT responses for the 3D trapezoidal hill model with computational domain boundaries placed at different $n_\delta = 1, 2, 4, 6, 8, 10$. The PETGEM solutions were calculated with $p = 1, 2$.

places at $n_\delta = 20$. It is worth mentioning that the numerical results and conclusions derived below remain valid for $p = 1$. Still, to preserve brevity, we focus on analyzing the $p = 2$ approximations with $n_\delta = 1, 4, 8$. Fig. 4 shows the obtained misfits for the resistivity component ρ_{yx} , where it can be seen that the least accurate solutions are those that were computed on meshes with boundaries placed at $n_\delta = 1$ away (this effect is also observable in apparent resistivities and phases depicted in Fig. 3). However, for meshes with boundaries placed at $n_\delta = 4, 8$, the numerical solutions exhibit better agreement with respect to the reference. More concretely, the misfit drops between 2 and 3 orders of magnitude for cases $n_\delta = 4, 8$ with respect to the case with boundary placed at $n_\delta = 1$. This pattern is similar for the resistivity component ρ_{xy} , which has been omitted to avoid over-plotting. Finally, we point that although the $n_\delta = 10$ case produces the most accurate apparent resistivity and phase values, the cases with boundaries at $n_\delta = 4, 6, 8$ can be competitive in function of the desirable accuracy.

3.1.2. Impact of high-order discretizations

As the second part of this experiment, we focus on studying the impact of high-order polynomial basis functions on meshes with an equivalent number of dof. Thus, we design a set of non-tailored meshes for $p = 1, 2, 3, 4$ and with the outer boundaries placed at $n_\delta = 4$. The resulting number of dof for all meshes is about 8×10^4 . These meshes have the same quality, same geometry and use the same meshing algorithm with slight variations in nodal positions. Again, we obtain the misfit ratios for each numerical scheme by direct comparison against a reference solution computed on h -fine mesh with $p = 6$ and outer boundaries places at $n_\delta = 10$.

The obtained misfit ratios for apparent resistivities (ρ_{yx}) and phases (ϕ_{yx}) are shown in Fig. 5. It can be seen the positive impact of high-order variants in the reduction of the numerical error. The most pronounced improvement occurs between $p = 1$ and $p = 2$. From there, the error reduction continues for $p = 3, 4$. Fig. 5 also depicts the error for each order of polynomial basis function, where it can be seen that the high-order basis exhibits a favorable impact on error control when

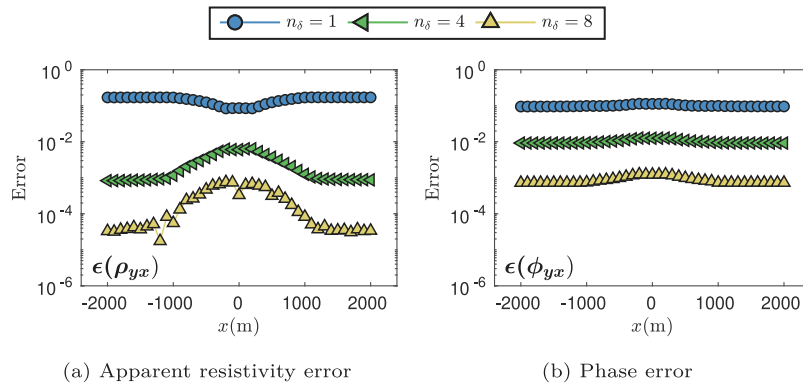


Fig. 4. Numerical errors of MT responses for the 3D trapezoidal hill model with computational domain boundaries placed at different $n_\delta = 1, 4, 8$. The PETGEM solutions were calculated with $p = 2$.

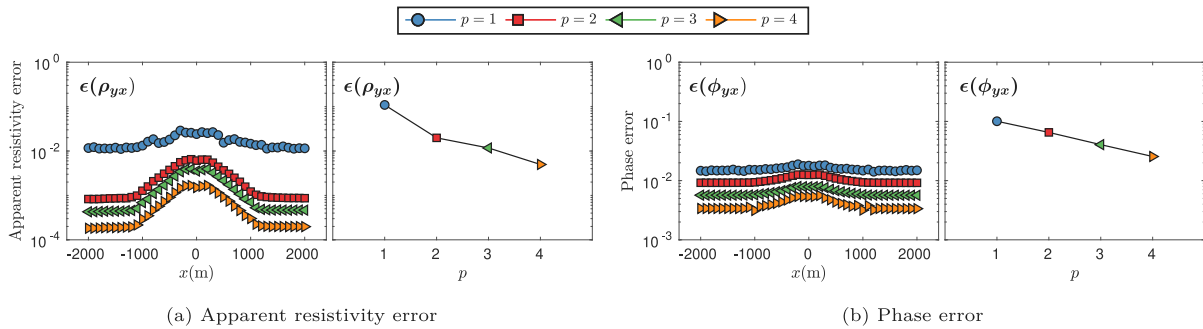


Fig. 5. Comparison of MT response errors for the 3D trapezoidal hill model using different polynomial order p . The PETGEM solutions were calculated on non-tailored meshes with $p = 1, 2, 3, 4$. The number of dof for all meshes is about 1×10^4 .

meshes with the equivalent number of dof are employed. Again, this behavior is similar for the resistivity component ρ_{xy} .

Given the results in these experiments, we conclude that the implementation of our 3D MT routine is correct. Also, our numerical results confirm that high-order polynomials can be up to ten times more accurate compared to first-order polynomials when the same number of dof are used (see Fig. 5). Given the reasonable misfit ranges for each p order and each n_δ value, we conclude that $p = 2$ with $n_\delta = 4$ provides the best compromise between misfit ratios and the number of dof. This conclusion is similar to that described in the context of active-source EM modeling (Schwarzbach et al., 2011; Grayver and Kolev, 2015; Castillo-Reyes et al., 2019; Rochlitz et al., 2019). Nonetheless, we acknowledge that our conclusions should be further corroborated for more complex modeling setups. Therefore, in the following experiments, we focus on completing the analysis of our parallel and high-order 3D MT algorithm.

3.2. Dublin test model 1 (DTM1)

As a second example, we consider the DTM1 proposed in the first 3D MT Dublin workshop. This 3D MT setup is suitable for verifying the code capabilities to modeling extreme situations such as a very wide range of periods and strong resistivity contrasts. The DTM1 consists of three different resistivity blocks in a homogeneous $\rho_{\text{earth}} = 100 \Omega \text{ m}$ half-space. The free-space resistivity is set to $\rho_{\text{air}} = 1 \times 10^8 \Omega \text{ m}$. The Fig. 6 depicts a sketch of the DTM1.

We consider the period range of 0.1 s to 10000 s taking four periods per decade. Following the recommendation for comparison proposed by the workshop, to perform the PETGEM simulations, we design tailored meshes for each period. We chose ≈ 7.5 points per skin-depth to control the characteristic element size in the computational grid and the boundaries are placed at eight skin-depth far away from the region of interest. The resulting mesh statistics are shown in Table 2. The

Table 2

Statistics of tailored meshes for DTM1. The periods, frequency, number of points per skin-depth (λ_δ), number of tetrahedral elements, number of dof, run-time, and memory for six relevant simulations are given.

Period (s)	Frequency (Hz)	λ_δ	Elements	dof	Run-time (min)	Memory (Gb)
0.1000	10.00	7.45	60665	403720	6.58	18.85
1	1.000	7.24	62819	420580	6.63	22.11
10	0.100	7.69	61660	417956	6.21	21.23
100	0.0100	7.67	61906	425096	6.29	25.02
1000	0.0010	7.71	62727	431356	6.27	26.74
10000	0.0001	7.64	62961	431836	6.64	26.93

PETGEM solutions for the central station ($x = y = 0 \text{ km}$) are shown in Fig. 7. Here, we compare our results against the unique numerical responses for that model computed with a low-order FE code presented in Miensopust et al. (2013). This FE reference solution was computed by Nuree Han and Tae Jong Le using the FE code by Nam et al. (2007). Overall, in Fig. 7 it can be seen an excellent match between both numerical solutions. The discrepancies are in diagonal elements of apparent resistivities and phases (ρ_{xx} , ρ_{yy} , ϕ_{xx} and ϕ_{yy}) for periods below 1 s where resistivity values are very small (more than eight orders of magnitude smaller than off-diagonal elements). As a result, the numerical solutions cannot capture them due to numerical errors. In fact, the diagonals elements contain structural information when the 3D effects are important. For the DTM1 and the station position under consideration, these 3D effects are present for periods above 1 s. We point out that these discrepancies are also showed in Miensopust et al. (2013) for other low-order numerical schemes (e.g., FD and IE methods). These results confirm that the EM response discrepancies for early periods are independent of the numerical method and its order.

It is worth mentioning here that the use of tailored meshes in conjunction with high-order polynomials can be beneficial for the

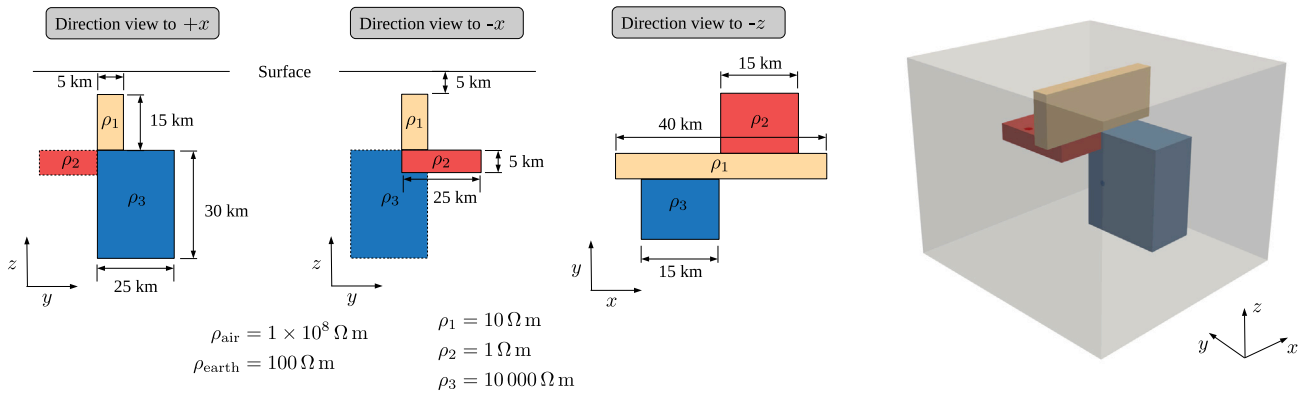


Fig. 6. Cross-section and 3D view of DTM1. The dimensions and resistivity values for each block are given.

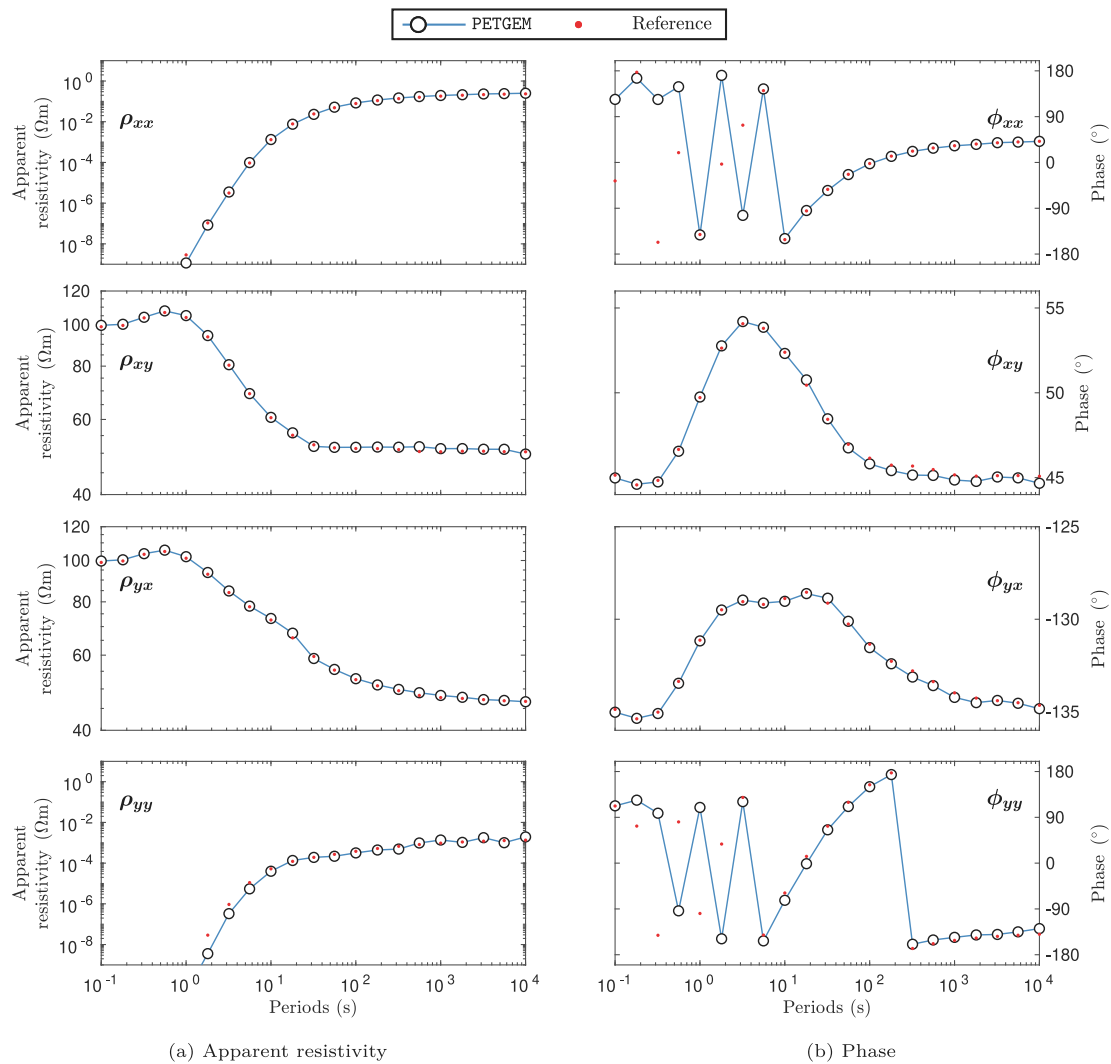


Fig. 7. Comparison of DTM1 responses between the FE code by Nam et al. (2007) and PETGEM for a station located at $x = y = 0$ km. The PETGEM solutions were calculated with $p = 2$.

solution of the problem under consideration. A close inspection of Table 2 shows that the number of elements and dof in the grid remains constant for all periods. Furthermore, the run-time to obtain the solution for each period is also constant. Last but not least, we point out the difference of elements between the reference grid and

our tailored meshes (e.g., 69 936 elements for reference solution against ≈ 61 000 elements for PETGEM computations). Furthermore, since we use polynomial basis functions $p = 2$, the resulting linear system of equations is much larger than those obtained in the reference. Given the results in these experiments, we conclude that our 3D MT modeling

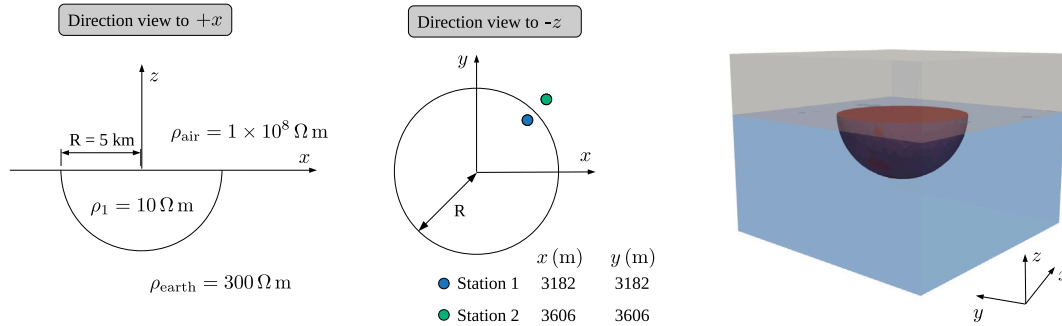


Fig. 8. Cross-section, plane, and 3D view of Dublin Test Model 2 (DTM2). The locations of the stations under consideration are included. Also, the resistivity values for each material are given.

Table 3

Statistics of tailored meshes for DTM2. The periods, frequency, number of points per skin-depth (λ_s), number of tetrahedral elements, number of dof, run-time, and memory for seven relevant simulations are given.

Period (s)	Frequency (Hz)	λ_s	Elements	dof	Run-time (min)	Memory (Gb)
0.0100	100.0	3.29	125 154	715 021	9.13	33.29
0.1000	10.00	3.23	121 733	739 320	9.42	34.87
1.00	1.000	3.57	126 311	776 358	9.98	36.31
10.0	0.100	3.56	127 629	770 352	9.42	35.62
100	0.010	3.60	126 604	770 454	9.69	35.67
1000	0.0010	3.58	125 633	732 836	9.49	33.91
10000	0.0001	3.71	125 857	752 478	9.76	35.03

routine is robust and capable of dealing with complex and realistic setups.

3.3. Dublin test model 2 (DTM2)

As a third example for our modeling algorithm, we chose the DTM2 which was proposed in the second 3D MT Dublin workshop. The original design purpose of this setup was to investigate how well the galvanic effects are dealt with in the modeling routines. The DTM2 corresponds to the model introduced by Groom and Bailey (1991), which is composed by an hemisphere $\rho_1 = 10 \Omega \text{ m}$ of radius $R = 5 \text{ km}$ embedded in a homogeneous $\rho_{\text{earth}} = 300 \Omega \text{ m}$ half-space. The free-space resistivity is set to $\rho_{\text{air}} = 1 \times 10^8 \Omega \text{ m}$. The Fig. 8 depicts a sketch of the DTM2. Again, we consider a very wide period range (from 0.01 to 10 000 s, with four periods per decade). As in the previous experiment, we design tailored meshes with ≈ 3 points per skin-depth for each period. Also, the boundaries are placed at eight skin-depth far away from the region of interest. The resulting mesh statistics are shown in Table 3.

For the DTM2, Miensopust et al. (2013) reported a vast responses comparison for two stations at the inner and outer boundary of the hemisphere (referred to as station 10 inside and station 18 outside in Miensopust et al. (2013), renamed here as station 1 and 2, respectively). We compare PETGEM responses against a low-order FE solution computed by Franke et al. (2007). It is important to state that the chosen FE reference solution corresponds to the more accurate approximation reported in Miensopust et al. (2013). More concretely, in Miensopust et al. (2013), the authors compared the synthetic responses against the analytic one at the galvanic limit. Therefore, we consider that comparing PETGEM responses against this FE reference follows a rigorous methodology.

The PETGEM solutions for station 1 and station 2 are shown in Fig. 9. For both stations, it can be seen an excellent agreement between PETGEM responses and the reference solution. For this modeling test, the positive impact tailored meshes and high-order polynomials remain valid. The number of elements and dof reported in Table 3 is

constant for all periods. Consequently, the required run-time to obtain the solution is also constant. Again, it is worth to mention here the difference in number of elements between the reference grid and the PETGEM tailored meshes (e.g., $\approx 300\,000$ elements for reference solution against $\approx 125\,000$ elements for PETGEM). In view of these numerical results, we conclude that our algorithm can solve 3D MT setups with both non-structured geometries and in the presence of galvanic effects.

3.4. Parallel performance analysis

Finally, the fourth test focuses on studying the parallel performance of the presented MT routine. We consider a fine mesh for the COMMEMI model introduced by Zhdanov et al. (1997), which is composed by three resistivity layers: $\rho_1 = 10 \Omega \text{ m}$, $\rho_2 = 100 \Omega \text{ m}$, and $\rho_3 = 0.1 \Omega \text{ m}$. Over imposed to this layered model, a resistive block $\rho_4 = 1 \Omega \text{ m}$ is embedded in the first layer (ρ_1). The dimensions of resistive block ρ_4 are 20 km in x -direction, 40 km in y -direction, and 10 km in z -direction. The free-space resistivity is set to $\rho_{\text{air}} = 1 \times 10^8 \Omega \text{ m}$. The Fig. 10 depicts a sketch of the COMMEMI model. In this case, we compute the solution for the horizontal components of the EM fields at 0.1 Hz on a tailored mesh with 68 619 elements. We consider the basis orders $p = 1, 2, 3, 4$, resulting in 86 606, 456 834, 1 316 541, and 2 871 584 dof, respectively.

We evaluate the code scalability on distributed-memory platforms by running the same problem size for a different number of CPU. We compute the speed-up ratios through

$$S = \frac{T_s}{T_N}, \tag{12}$$

where T_s is the serial run-time; T_N is the parallel run-time; and N is the total number of CPUs. Furthermore, we measure the fraction of time for which a CPU is usefully utilized. This performance metric, also referred to as parallel efficiency, corresponds to the ratio of S with respect to N . We compute the parallel efficiency through

$$E = \frac{S}{N} = \frac{T_s}{N \cdot T_N}. \tag{13}$$

The obtained speed-up and parallel efficiency ratios for the MUMPS solver are shown in Table 4. In our experiments, the serial run-time used as reference is the resulting from computations with 48 CPUs (1 computing node). The excellent performance ratios for high-order simulations can be seen due to the higher workload per CPU (e.g., the quadrature order for numerical integration increases in a proportional ratio to the polynomial basis order). Fig. 11 depicts the obtained speed-up and the parallel efficiency for polynomial basis functions of order $p = 1, 2, 3, 4$. We obtained a near-linear speed-up growth for up to 1 008 CPUs. From this number of CPUs, the speed-up ratios stop its almost linear gain due to the execution becomes dominated by the communication between processing units (e.g., messages exchange to perform the parallel solution of the linear system of equations). Nevertheless, the speed-up ratios keep increasing constantly, and we obtained significant run-time reductions for more than a thousand CPUs. Furthermore,

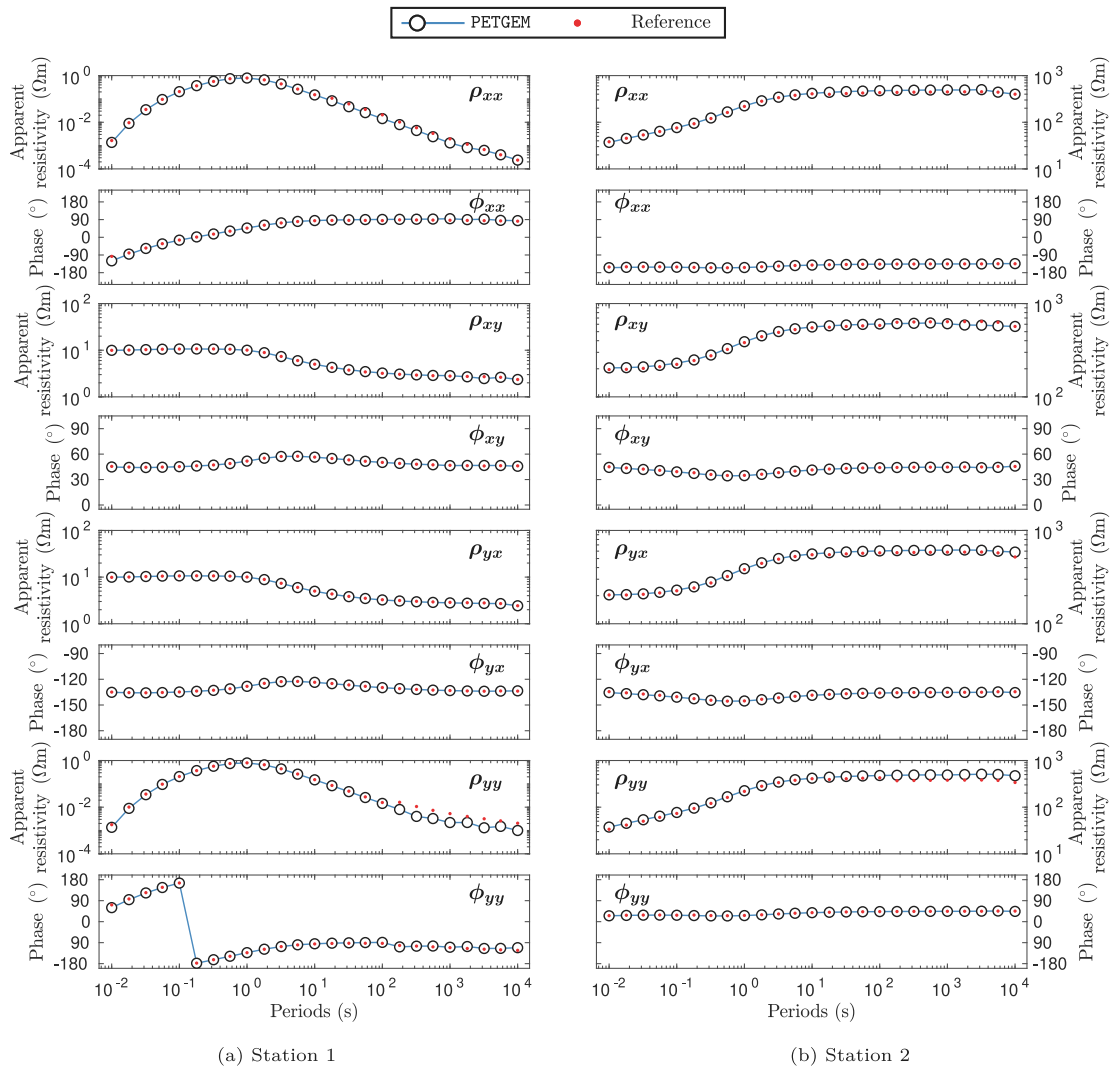


Fig. 9. Comparison of DTM2 responses between the FE code by Franke et al. (2007) and PETGEM. See Fig. 8 for more details about station locations. The PETGEM solutions were calculated with $p = 2$.

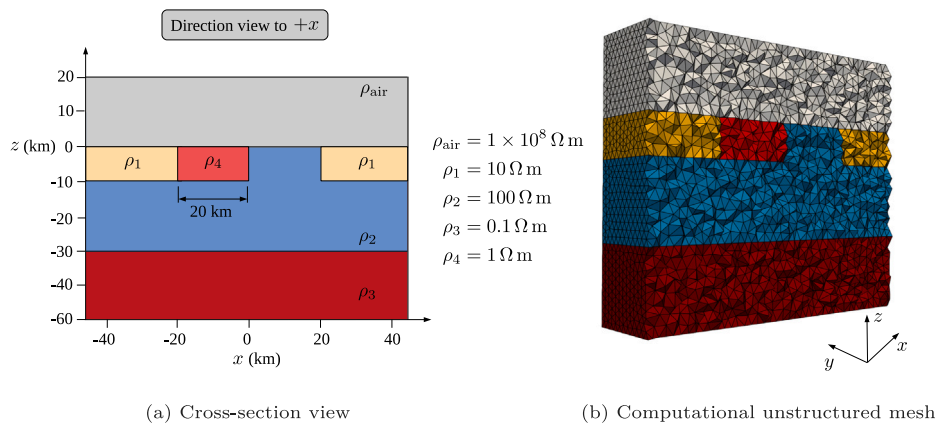


Fig. 10. 3D COMMEMI model used for PETGEM performance analysis.

Fig. 11 shows the percent of parallel efficiency for each order of polynomial basis function. It can be seen that although higher-order polynomials increase the run-time, they offer better parallel efficiency ratios (see Table 4). For example, a 15.13 speed-up on 1 008 CPUs for $p = 1$ corresponds to a efficiency of 72.05 %. This ratio means that,

on average, over the course of the execution, each of the CPUs is idle about 28 %. For basis function $p = 2$ it is a bit different, where a speed-up of 19.19 on the same number of CPUs is obtained, resulting in an efficiency ratio of 91.86 % which indicates that each CPUs is idle about 8 % during the execution. This conclusion is consistent for

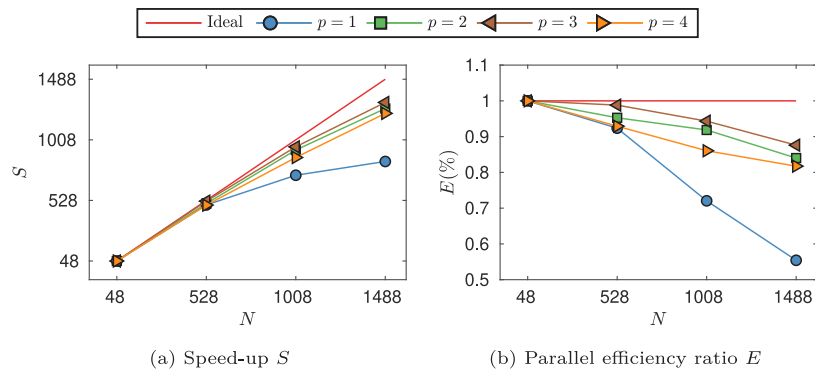


Fig. 11. Parallel efficiency results for the COMMEMI model. Results for $p = 1, 2, 3, 4$ are given. The red line depicts the theoretical ideal performance assuming 100% parallel efficiency. (For interpretation of the references to color in this figure legend, the reader is referred to the web version of this article.)

Table 4

Scalability results for different number of CPU and $p = 1, 2, 3, 4$ on distributed-memory architectures. The run-time (minutes), the speed-up S , and the parallel efficiency E (percent) are given.

CPU	48	528	1008	1488
$p = 1$ with 86 606 dof				
Run-time	6.97	0.68	0.46	0.40
S	–	10.16	15.13	17.18
E (%)	–	92.36	72.05	55.42
$p = 2$ with 456 834 dof				
Run-time	36.89	3.52	1.91	1.41
S	–	10.48	19.19	26.11
E (%)	–	95.27	91.86	84.01
$p = 3$ with 1 316 541 dof				
Run-time	105.98	9.74	5.34	3.90
S	–	10.87	19.81	27.16
E (%)	–	98.81	94.33	87.61
$p = 4$ with 2 871 584 dof				
Run-time	238.68	23.35	13.20	9.41
S	–	10.22	18.07	25.34
E (%)	–	92.91	86.05	81.74

a still higher number of CPUs and polynomial orders $p = 3, 4$. We state that the reported run-time depends mostly on the solver-type. Since we use general-purpose solver implementations, no special efforts were undertaken to minimize run-time, as this is an entire different task.

4. Discussion

The development of 3D MT modeling routines has increased in the last decade. As a result, today, there are several codes available to solve arbitrarily setups of the 3D MT problem and obtain reasonable-looking results. However, most of the current algorithms for MT modeling lack an open-source development environment, which makes it hard for other users to study, adapt, and extend the code features to their own needs. Also, regardless of the type of meshes used, most of these algorithms use low-order numerical methods, and few of them support parallelism on modest multi-core architectures. These are the core motivations for this study and the introduction of a new PETGEM version.

To demonstrate the robustness of our high-order algorithm, we compute the solutions for a set of challenging 3D MT setups. Overall, it can be seen an excellent match between reference solutions and PETGEM responses. The first test is based on the 3D hill model, and its main purpose is to study the impact of tailored meshes, the distance between computational core and artificial boundaries, and the accuracy of high-order polynomial basis functions. The obtained EM responses have mostly a relative error of less than 1–3%. The PETGEM simulations on tailored meshes with boundaries placed at different skin-depths

yield a general EM behavior consistent with previously computed FE solutions. However, the most accurate solutions correspond to that with boundaries placed from at least four skin-depths. These results confirm the importance of the distance between the artificial boundaries and the region of interest. Furthermore, the 3D hill model simulations performed on meshes with an equivalent number of dof yields a positive impact of high-order variants in reducing the numerical error. More concretely, in our experiments, it can be observed that high-order polynomial basis functions can be up to ten times more accurate compared to low-order polynomial basis functions (see Fig. 5). The second model under consideration is the DTM1, which is more realistic than the previous one in terms of scale and physical parameters (e.g., large resistivity contrasts and large periods of time). For this model, we design tailored meshes for each period. The cross-validation between PETGEM and the low-order FE code by Nam et al. (2007) yields a similar EM pattern. The main discrepancies between both approximations are in diagonal elements of apparent resistivities and phases for early periods (e.g., below 1 s). However, these differences are also presented in other numerical solutions reported in Miensopust et al. (2013). Therefore, we consider these results to be correct because comparing different codes which use different numerical methods and different grids is ideal to address the topic of validation. The third test case is the DTM2 which also exhibits large periods of time. We compute the apparent resistivities and phases for two stations using tailored meshes. Here, we compare our results against the low-order FE code by Franke et al. (2007). The cross-validation between both numerical approximations yields an excellent agreement.

According to one of the main findings of this study, the mesh design is a complex and time-consuming process, but its know-how is fundamental for future modeling tasks and developments (e.g., EM inversion routines). As a result, adaptive meshing has already been investigated in geophysical electromagnetics (Plessix et al., 2007; Schwarzbach et al., 2011; Key, 2016; Castillo-Reyes et al., 2018, 2019). Such meshing rules take into account the physics of EM fields computation with its diffusive behavior. The main conclusions of these works confirm that ad-hoc meshing strategies are needed to increase the modeling routine's flexibility and provide accurate solutions in a feasible run-time. Therefore, we built tailored meshes based on the rules proposed by Castillo-Reyes et al. (2019), which were originally designed and evaluated for active-source electromagnetic modeling (e.g., CSEM). The core of this meshing process follows the skin-depth principle as the main quality criteria to determine the characteristic mesh sizes for each order of polynomial basis functions and each period of time. Our numerical results confirm that the rigorous application of these meshing rules can be beneficial for 3D MT modeling in terms of run-time and accuracy (e.g., for DTM1 and DTM2 the number of dof and run-time remains constant for each period, see Tables 2 and 3). Also, we point out the difference of number of elements between the reference grids and our ad-hoc meshes for DTM1 and DTM2. Using

tailored meshes and HPC, we achieved a considerable reduction in the run-times compared with those reported in Miensopust et al. (2013). We acknowledge that this run-time improvement is due to the use of HPC, one clearly evident differentiator in the state-of-the-art of 3-MT modeling.

In our numerical experiments, the accuracy obtained with each basis function is consistent with the theoretical definition. Also, the high-order polynomial degrees require fewer dof to attain a given error level in comparison with the low-order case. However, this accuracy improvement has a cost. The computational implementation of HEFEM and its parallelization are technically complex. Also, the use of high-order elements decrease the sparsity pattern of the resulting linear system due the number of dof per element is larger. Then, high-order schemes demands more memory. Furthermore, the computation of the element integrals is more expensive for high-order basis functions (e.g., the quadrature order for numerical integration increases in a proportional ratio to the polynomial basis order). Consequently, the run-time for linear system assembly is also increased. However, the used solver is the main discriminator in terms of run-time, memory consumption, and parallel efficiency. In this paper, we use the MUMPS direct solver to obtain the solutions for the proposed 3D MT models. Furthermore, we investigate the computational efficiency of the code for the solution of large-scale modeling setups. When high-order polynomial basis functions and more than a thousand CPUs are employed, the performance scalability study shows that PETGEM offers excellent parallel efficiency.

We state that the used performance metrics to compare our numerical solutions are those available in Miensopust et al. (2013) (e.g., run-time and number of mesh cells). The authors did not report the memory needs. Validating the correctness and efficiency of 3D codes is a difficult task, and it is essential to have easily accessible benchmark models with reliable and reproducible solutions. Therefore, in our study, we promote open practices, including sharing of code and data. We hope that these results may be useful for the entire MT community and more robust comparisons in the future (e.g., modeling tests that include real data).

5. Conclusions

We have presented a new high-order and parallel modeling routine for arbitrary 3-D MT setups. This algorithm is based on and extends the PETGEM code, which was initially developed for 3-D marine CSEM problems. To verify the robustness, accuracy, and computational efficiency of this new version code, we solve a set of reference models within the MT community. These models exhibit large resistivity contrasts, a wide range of periods, and relatively complex geometries, making them challenging and ideal to address the topic of validation.

A 3-D hill model is used as first example to verify our implementation and study the impact of tailored meshes and high-order discretizations. The second and third example correspond to realistic and complex 3-D MT setups, namely the DTM1 and DTM2. These models and its corresponding MT responses are open-source, allowing an independent cross-validation of our numerical results. In all test cases, the high-order discretizations in conjunction with tailored meshes show excellent accuracy. Furthermore, by using tailored meshes and HPC, the obtained run-times have proven to be highly competitive for the solution of realistic synthetic 3D MT setups. Then, we conclude that a proper discretization is crucial not only for accurate results but also to obtain solutions in a feasible run-time. Also, a scalability test demonstrates that PETGEM offers an excellent efficiency in HPC clusters. Nevertheless, we state that code performance depends on the input model, solver-type, and computational architecture.

In view of our numerical results, we conclude that PETGEM features satisfy modeling requirements of challenging and arbitrarily 3-D MT setups using both modest multi-core architectures and large-scale parallel computing clusters. We believe that the upgraded version of our

modeling tool and numerical experiments prove useful for geophysicists interested in arbitrary passive-source EM modeling (also applicable for active-source EM methods). Our future research aims to compare synthetic 3-D MT responses against experimental data in a geothermal exploration context. Also, we intend to perform simulations for models that include anisotropy.

CRedit authorship contribution statement

Octavio Castillo-Reyes: Conceived the study, Contributed to the parallel implementation, math background, mesh generation, PETGEM simulations, Wrote the manuscript. **David Modesto:** Contributed to the magnetotelluric math background, Critically revised the manuscript. **Pilar Queralt:** Analyzed and interpreted the modeling results, Supervised the overall study, Critically revised the manuscript. **Alex Marcuello:** Analyzed and interpreted the modeling results, Supervised the overall study, Critically revised the manuscript. **Juanjo Ledo:** Analyzed and interpreted the modeling results, Supervised the overall study, Critically revised the manuscript. **Adrian Amor-Martin:** Contributed to the numerical background about high-order edge finite element method. **Josep de la Puente:** Contributed to the magnetotelluric math background, Critically revised the manuscript. **Luis Emilio Garcia-Castillo:** Contributed to the numerical background about high-order edge finite element method.

Declaration of competing interest

The authors declare that they have no known competing financial interests or personal relationships that could have appeared to influence the work reported in this paper.

Code and data availability

The resulting MT responses ($p = 1, 2, 3, 4, 5, 6$) for the models presented here, as well as all mesh files to rerun the different models with PETGEM and reproduce the shown results are available at Zenodo (10.5281/zenodo.5805053). The PETGEM code is freely available at the home page (<https://petgem.bsc.es/>), at the PyPI repository (<https://pypi.org/project/petgem/>), at the GitHub site (<https://github.com/oastilloreyes/petgem>). In all cases, the code is supplied to ease the immediate execution on Linux platforms. User's manual and technical documentation (developer's guide) are provided in the PETGEM archive.

Acknowledgments

This project has been 65% cofinanced by the European Regional Development Fund (ERDF) through the Interreg V-A Spain–France–Andorra program (POCTEFA2014-2020). POCTEFA aims to reinforce the economic and social integration of the French–Spanish–Andorran border. Its support is focused on developing economic, social and environmental cross-border activities through joint strategies favoring sustainable territorial development. BSC authors received funding from the European Union's Horizon 2020 programme, grant agreement N°828947 and N°777778, and from the Mexican Department of Energy, CONACYT-SENER Hidrocarburos grant agreement N°B-S-69926.

Appendix A. Computation of impedance and apparent resistivities

Electric and magnetic fields are related with the linear law

$$\mathbf{E} = \mathbb{Z}\mathbf{H}, \quad (\text{A.1})$$

where \mathbb{Z} is the model impedance that, in the (x, y) plane, is defined as

$$\mathbb{Z} = \begin{pmatrix} v_{xx} & v_{xy} \\ v_{yx} & v_{yy} \end{pmatrix}. \quad (\text{A.2})$$

The four components in Eq. (A.2) can be evaluated by solving the system

$$\begin{aligned} \mathbf{E}_1 &= \mathbb{Z}\mathbf{H}_1, \\ \mathbf{E}_2 &= \mathbb{Z}\mathbf{H}_2, \end{aligned} \quad (\text{A.3})$$

where \mathbf{E}_1 and \mathbf{H}_1 are the electromagnetic fields obtained when polarizing the electric field along the x direction. Analogously, \mathbf{E}_2 and \mathbf{H}_2 result from the y -polarization. Note that the system (A.3) can be solved analytically using the Cramer's rule. From the impedance components, the common quantities of interest to be evaluated in MT applications are the apparent resistivities ρ_{ij} and phases ϕ_{ij} for $i, j = \{x, y\}$, which are defined by

$$\rho_{ij} = \frac{|v_{ij}|^2}{\mu\omega}, \quad (\text{A.4})$$

$$\phi_{ij} = \tan^{-1} \left(\frac{\text{Im}(v_{ij})}{\text{Re}(v_{ij})} \right). \quad (\text{A.5})$$

Appendix B. Implementation details of the variational formulation

We discretize Eqs. (9) and (10) into the different elements that conform the tetrahedral mesh. We use reference elements to alleviate the computational effort since some of the calculations might be precomputed in this master element and then mapped to the real elements. We use the well-known covariant and contravariant Piola mappings (Rognes et al., 2009), with Jacobian matrix J , yielding for each element

$$\begin{aligned} \int_{\Omega} (\nabla \times \mathbf{v}(x, y, z)) \cdot (\nabla \times \mathbf{E}(x, y, z)) d\Omega &= \int_{\tilde{\Omega}} \frac{1}{\det J} J^T (\tilde{\nabla} \times \tilde{\mathbf{v}}(\tilde{x}, \tilde{y}, \tilde{z})) \\ &\quad \times \frac{1}{\det J} J^T (\tilde{\nabla} \times \tilde{\mathbf{E}}(\tilde{x}, \tilde{y}, \tilde{z})) \\ &\quad \times \det J d\tilde{\Omega}, \end{aligned} \quad (\text{B.1})$$

$$\begin{aligned} \int_{\Omega} i\omega\mu\sigma\mathbf{v}(x, y, z) \cdot \mathbf{E}(x, y, z) d\Omega &= \int_{\tilde{\Omega}} i\omega\mu\sigma (J^{-1}\tilde{\mathbf{v}}(\tilde{x}, \tilde{y}, \tilde{z})) \\ &\quad \cdot (J^{-1}\tilde{\mathbf{E}}(\tilde{x}, \tilde{y}, \tilde{z})) \det J d\tilde{\Omega}, \end{aligned} \quad (\text{B.2})$$

where we have used $\tilde{\cdot}$ to denote everything defined in the reference element. We have assumed without loss of generality straight elements making J independent of the coordinates.

Regarding the linear form $l(\cdot)$ from Eq. (10), we need to perform a two-dimensional integral on the boundary $\partial\Omega$. We use the curl-conforming properties of the basis functions and obtain their tangential component, i.e.,

$$\begin{aligned} \int_{\Gamma} \mathbf{v}(x, y, z) \left(\mathbf{n} \times \hat{\mathbf{H}}(x, y, z) \right) d\Gamma &= \int_{\tilde{\Gamma}} J^{-1} (\tilde{\mathbf{n}} \times \tilde{\mathbf{v}}(\tilde{x}, \tilde{y}, \tilde{z})) \times \tilde{\mathbf{n}} \\ &\quad \cdot \left(\mathbf{n} \times \hat{\mathbf{H}}(x, y, z) \right) \det J d\tilde{\Gamma}, \end{aligned} \quad (\text{B.3})$$

since the basis functions that does not belong to the face yield zero tangential component on that face. We assemble that term directly to the dof of the element. We need to use two-dimensional integration points on each face that need to be mapped either into the reference element (for the evaluation of $\tilde{\mathbf{v}}$) or into the real element (for the evaluation of $\hat{\mathbf{H}}$). The mapping now is from 2D to 3D, so we use the jacobian matrix $J_f \in \mathbb{R}^{2 \times 3}$ for the mapping

$$\begin{bmatrix} \xi \\ \eta \\ \zeta \end{bmatrix} = J_f^T \begin{bmatrix} \tilde{x}^{2D} \\ \tilde{y}^{2D} \end{bmatrix} + \begin{bmatrix} \xi_1 \\ \eta_1 \\ \zeta_1 \end{bmatrix} \quad (\text{B.4})$$

being $(\tilde{\cdot})^{2D}$ the integration points on a 2D triangle; $[\xi, \eta, \zeta]$ is $[\tilde{x}, \tilde{y}, \tilde{z}]$ and $[x, y, z]$ when we define the mapping to the 3D face in the reference and real element respectively; and $[\xi_1, \eta_1, \zeta_1]$ is the first point of the face used to realize the mapping.

References

- Amestoy, P.R., Guermouche, A., L'Excellent, J.-Y., Pralet, S., 2006. Hybrid scheduling for the parallel solution of linear systems. *Parallel Comput.* 32 (2), 136–156.
- Avdeeva, A., Moorkamp, M., Avdeev, D., Jegen, M., Miensopust, M., 2015. Three-dimensional inversion of magnetotelluric impedance tensor data and full distortion matrix. *Geophys. J. Int.* 202 (1), 464–481.
- Balay, S., Abhyankar, S., Adams, M.F., Brown, J., Brune, P., Buschelman, K., Dalcin, L., Eijkhout, V., Gropp, W.D., Kaushik, D., Knepley, M.G., McInnes, L.C., Rupp, K., Smith, B.F., Zampini, S., Zhang, H., Zhang, H., 2016. PETSc Web site. URL: <http://www.mcs.anl.gov/petsc>.
- Bondeson, A., Rylander, T., Ingelström, P., 2012. *Computational Electromagnetics*. Springer, pp. 224–227.
- Börner, R.-U., 2010. Numerical modelling in geo-electromagnetics: Advances and challenges. *Surv. Geophys.* 31 (2), 225–245.
- Campanyà, J., Ledo, J., Queralt, P., Marcuello, A., Liesa, M., Muñoz, J.A., 2012. New geoelectrical characterisation of a continental collision zone in the West-Central Pyrenees: Constraints from long period and broadband magnetotellurics. *Earth Planet. Sci. Lett.* 333, 112–121.
- Castillo-Reyes, O., de la Puente, J., a Cela, J.M., 2018. PETGEM: A parallel code for 3D CSEM forward modeling using edge finite elements. *Comput. Geosci.* 119, 126–136. <http://dx.doi.org/10.1016/j.cageo.2018.07.005>.
- Castillo-Reyes, O., de la Puente, J., García-Castillo, L.E., Cela, J.M., 2019. Parallel 3D marine controlled-source electromagnetic modeling using high-order tetrahedral Nédélec elements. *Geophys. J. Int.* 219, 39–65. <http://dx.doi.org/10.1093/gji/ggz285>.
- Chave, A.D., Jones, A.G., 2012. *The Magnetotelluric Method: Theory and Practice*. Cambridge University Press, p. 20.
- Colton, D., Kress, R., 2013. *Integral Equation Methods in Scattering Theory*. SIAM, pp. 108–136.
- Du, H.-K., Ren, Z.-Y., Tang, J.-T., 2016. A finite-volume approach for 2D magnetotellurics modeling with arbitrary topographies. *Stud. Geophys. Geod.* 60 (2), 332–347.
- Eymard, R., Gallouët, T., Herbin, R., 2000. Finite volume methods. In: *Handbook of Numerical Analysis*, Vol. 7. Elsevier, pp. 713–1018.
- Farquharson, C.G., Miensopust, M.P., 2011. Three-dimensional finite-element modelling of magnetotelluric data with a divergence correction. *J. Appl. Geophys.* 75 (4), 699–710.
- Franke, A., Börner, R., Spitzer, K., 2007. 3D finite element simulation of magnetotelluric fields using unstructured grids. In: *Proceedings of The 22nd Colloquium Of Electromagnetic Depth Research*. pp. 27–33.
- Geuzaine, C., Remacle, J.-F., 2008. Gmsh: a three-dimensional finite element mesh generator with built-in pre-and post-processing facilities (2008). URL: <http://www.geuz.org/gmsh>.
- Grayver, A.V., Kolev, T.V., 2015. Large-scale 3D geoelectromagnetic modeling using parallel adaptive high-order finite element method. *Geophysics* 80 (6), E277–E291.
- Groom, R.W., Bailey, R., 1991. Analytic investigations of the effects of near-surface three-dimensional galvanic scatterers on MT tensor decompositions. *Geophysics* 56 (4), 496–518.
- Guo, Z., Egbert, G., Dong, H., Wei, W., 2020. Modular finite volume approach for 3D magnetotelluric modeling of the Earth medium with general anisotropy. *Phys. Earth Planet. Inter.* 309, 106585.
- Jahandari, H., Ansari, S., Farquharson, C.G., 2017. Comparison between staggered grid finite-volume and edge-based finite-element modelling of geophysical electromagnetic data on unstructured grids. *J. Appl. Geophys.* 138, 185–197.
- Jin, J.-M., 2015. *The Finite Element Method in Electromagnetics*. John Wiley & Sons, pp. 19–26, 292–298.
- Kelbert, A., Meqbel, N., Egbert, G.D., Tandon, K., 2014. ModEM: A modular system for inversion of electromagnetic geophysical data. *Comput. Geosci.* 66, 40–53.
- Key, K., 2016. MARE2DEM: a 2-D inversion code for controlled-source electromagnetic and magnetotelluric data. *Geophys. J. Int.* 207 (1), 571–588.
- Kordy, M., Wannamaker, P., Maris, V., Cherkov, E., Hill, G., 2016. 3-D magnetotelluric inversion including topography using deformed hexahedral edge finite elements and direct solvers parallelized on SMP computers-Part I: forward problem and parameter Jacobians. *Geophys. J. Int.* 204 (1), 74–93.
- Kun, Z., Hao, D., Jia-Yong, Y., Qing-Tian, L., Wen-Bo, W., Yu-Xian, H., 2013. A NLCC 3-D inversion method of magnetotellurics with parallel structure. *Chin. J. Geophys.* 56 (6), 754–765.
- Kunz, K.S., Luebbers, R.J., 1993. *The Finite Difference Time Domain Method for Electromagnetics*. CRC Press, pp. 11–27.
- Ledo, J., Queralt, P., Martí, A., Jones, A.G., 2002. Two-dimensional interpretation of three-dimensional magnetotelluric data: an example of limitations and resolution. *Geophys. J. Int.* 150 (1), 127–139.
- Liu, C., Ren, Z., Tang, J., Yan, Y., 2008. Three-dimensional magnetotellurics modeling using edge based finite-element unstructured meshes. *Appl. Geophys.* 5 (3), 170–180.
- Mackie, R.L., Smith, J.T., Madden, T.R., 1994. Three-dimensional electromagnetic modeling using finite difference equations: The magnetotelluric example. *Radio Sci.* 29 (4), 923–935.

- Miensepost, M.P., Queral, P., Jones, A.G., modellers, D.M., 2013. Magnetotelluric 3-D inversion—a review of two successful workshops on forward and inversion code testing and comparison. *Geophys. J. Int.* 193 (3), 1216–1238.
- Nam, M.J., Kim, H.J., 2010. 3D MT inversion using an edge finite element modeling algorithm. *Geosyst. Eng.* 13 (2), 43–52.
- Nam, M.J., Kim, H.J., Song, Y., Lee, T.J., Son, J.-S., Suh, J.H., 2007. 3D magnetotelluric modelling including surface topography. *Geophys. Prospect.* 55 (2), 277–287.
- Nam, M.J., Kim, H.J., Song, Y., Lee, T.J., Suh, J.H., 2008. Three-dimensional topography corrections of magnetotelluric data. *Geophys. J. Int.* 174 (2), 464–474.
- Nédélec, J.-C., 1980. Mixed finite elements in R3. *SIAM J. Numer. Anal.* 17 (3), 315–341.
- Piña-Varas, P., Ledo, J., Queral, P., Marcuello, A., Bellmunt, F., Ogaya, X., Pérez, N., Rodríguez-Losada, J., 2015. Vertical collapse origin of Las Cañadas caldera (Tenerife, Canary Islands) revealed by 3-D magnetotelluric inversion. *Geophys. Res. Lett.* 42 (6), 1710–1716.
- Plessix, R.-E., Darnet, M., Mulder, W., 2007. An approach for 3D multisource, multifrequency CSEM modeling. *Geophysics* 72 (5), SM177–SM184.
- Queral, P., Jones, A.G., Ledo, J., 2007. Electromagnetic imaging of a complex ore body: 3D forward modeling, sensitivity tests, and down-mine measurements. *Geophysics* 72 (2), F85–F95.
- Ren, Z., Kalscheuer, T., Greenhalgh, S., Maurer, H., 2013. A goal-oriented adaptive finite-element approach for plane wave 3-D electromagnetic modelling. *Geophys. J. Int.* 194 (2), 700–718.
- Rivera-Rios, A.M., Zhou, B., Heinson, G., Krieger, L., 2019. Multi-order vector finite element modeling of 3D magnetotelluric data including complex geometry and anisotropy. *Earth Planets Space* 71 (1), 1–25.
- Rochlitz, R., Skibbe, N., Günther, T., 2019. custEM: Customizable finite-element simulation of complex controlled-source electromagnetic data. *Geophysics* 84 (2), F17–F33.
- Rognes, M.E., Kirby, R.C., Logg, A., 2009. Efficient assembly of $H(\text{div})$ and $H(\text{curl})$ conforming finite elements. *SIAM J. Numer. Anal.* 47 (3), 4130–4151. <http://dx.doi.org/10.1137/08073901X>. URL: <https://epubs.siam.org/doi/abs/10.1137/08073901X>.
- Schwarzbach, C., Börner, R.-U., Spitzer, K., 2011. Three-dimensional adaptive higher order finite element simulation for geo-electromagnetics—a marine CSEM example. *Geophys. J. Int.* 187 (1), 63–74.
- Singh, A., Dehiya, R., Gupta, P.K., Israil, M., 2017. A MATLAB based 3D modeling and inversion code for MT data. *Comput. Geosci.* 104, 1–11.
- Siripunvaraporn, W., Egbert, G., Lenbury, Y., 2002. Numerical accuracy of magnetotelluric modeling: a comparison of finite difference approximations. *Earth Planets Space* 54 (6), 721–725.
- Ting, S.C., Hohmann, G.W., 1981. Integral equation modeling of three-dimensional magnetotelluric response. *Geophysics* 46 (2), 182–197.
- Varilsuha, D., Candansayar, M.E., 2018. 3D magnetotelluric modeling by using finite-difference method: Comparison study of different forward modeling approaches. *Geophysics* 83 (2), WB51–WB60.
- Vilamajó, E., Queral, P., Ledo, J., Marcuello, A., 2013. Feasibility of monitoring the Hontomín (Burgos, Spain) CO₂ storage site using a deep EM source. *Surv. Geophys.* 34 (4), 441–461.
- Wannamaker, P.E., 1991. Advances in three-dimensional magnetotelluric modeling using integral equations. *Geophysics* 56 (11), 1716–1728.
- Xiao, T., Liu, Y., Wang, Y., Fu, L.-Y., 2018. Three-dimensional magnetotelluric modeling in anisotropic media using edge-based finite element method. *J. Appl. Geophys.* 149, 1–9.
- Zhang, J., Liu, J., Feng, B., Guan, J., Liu, Z., et al., 2021. Three-dimensional magnetotelluric modeling using the finite element model reduction algorithm. *Comput. Geosci.* 104750.
- Zhdanov, M., Varentsov, I.M., Weaver, J., Golubev, N., Krylov, V., 1997. Methods for modelling electromagnetic fields results from COMMEMI—the international project on the comparison of modelling methods for electromagnetic induction. *J. Appl. Geophys.* 37 (3–4), 133–271.
- Zhu, X., Liu, J., Cui, Y., Gong, C., 2021. An efficient parallel algorithm for 3D magnetotelluric modeling with edge-based finite element. *Comput. Geosci.* 25 (1), 1–16.